INTERNATIONAL JOURNAL FOR NUMERICAL METHODS IN FLUIDS
Int. J. Numer. Meth. Fluids 2002; **39**:361–390 (DOI: 10.1002/fld.286)

A comparison of time integration methods in an unsteady low-Reynolds-number flow

Petri Majander*,† and Timo Siikonen‡

Laboratory of Applied Thermodynamics, Helsinki University of Technology, P.O. Box 4400, Finland

SUMMARY

This paper describes three different time integration methods for unsteady incompressible Navier–Stokes equations. Explicit Euler and fractional-step Adams–Bashford methods are compared with an implicit three-level method based on a steady-state SIMPLE method. The implicit solver employs a dual time stepping and an iteration within the time step. The spatial discretization is based on a co-located finite-volume technique. The influence of the convergence limits and the time-step size on the accuracy of the predictions are studied. The efficiency of the different solvers is compared in a vortex-shedding flow over a cylinder in the Reynolds number range of 100–1600. A high-Reynolds-number flow over a biconvex airfoil profile is also computed. The computations are performed in two dimensions. At the low-Reynolds-number range the explicit methods appear to be faster by a factor from 5 to 10. In the high-Reynolds-number case, the explicit Adams–Bashford method and the implicit method appear to be approximately equally fast while yielding similar results. Copyright © 2002 John Wiley & Sons, Ltd.

KEY WORDS: unsteady incompressible Navier–Stokes; vortex shedding; pressure correction; SIMPLE; fractional-step method

1. INTRODUCTION

The main division of the time advancement schemes of numerical Navier–Stokes solutions lies between explicit and implicit methods. With an explicit scheme, the stability criterion for a linear convection equation states that a Courant–Friedrich–Levy number is lower than one, i.e. $\mathrm{CFL}=u\Delta t/\Delta x\leqslant 1$ in each co-ordinate direction, which means that a flow cannot advance more than one grid spacing or control-volume diameter during one time step. Some predictor-corrector schemes, like Runge–Kutta schemes, may violate this restriction within the order of magnitude [1].

Owing to the time-step restrictions, the implicit methods have been especially developed for steady-state computations. The implicit methods have an advantage of being typically

* Correspondence to: P. Majander, Laboratory of Applied Thermodynamics, Department of Mechanical Engineering, Helsinki University of Technology, P.O. Box 4400, Helsinki, Finland.
† Research Scientist, E-mail: petri.majander@hut.fi
‡ Professor, E-mail: timo.siikonen@hut.fi.

Contract/grant sponsor: Academy of Finland.

Received April 2000
Revised October 2001

unconditionally stable in terms of linear analysis. Even for time-dependent problems, the time-step restriction imposed by the stability condition may be too stringent compared to that warranted by the time scales of the solution. Choi and Moin computed direct numerical simulation over the riblets with an implicit method and they found a saving factor of five in the CPU time compared to semi-implicit calculation [2].

In this study, a vortex-shedding flow over a cylinder is computed by using two explicit schemes and one implicit scheme, and a comparison is conducted between the results and especially between the efficiency in computational effort. An explicit Euler method leads to a similar algorithm to that of Harlow and Welch [3], who used a staggered grid and a difference method. All the solvers of this study are written in a co-located finite-volume formulation.

Unsteady problems are often solved such that different terms of Navier–Stokes equations can be advanced in a different manner. This idea was introduced by Chorin [4], and various methods of this sort are often known generically as fractional-step methods. A fully explicit version utilizing an Adams–Bashford scheme for convective and diffusive terms is used in this study.

Probably, the most popular algorithm for solving incompressible Navier–Stokes equations is known by the acronym, SIMPLE, from semi-implicit method for pressure-linked equations [5]. This method was originally developed for steady-state computations, where implicit methods are superior. SIMPLE and its variants form the basic solver in many commercial programs.

An implicit SIMPLE code utilizing a local time stepping is derived and it is turned into a time-accurate version, where the solution is iterated within the time step.

In this study, different methods are compared in a vortex-shedding cylinder flow case in a Reynolds number range from 100 to 1600. The results and the efficiency of the different schemes in the computations are compared. The influence of the convergence limits and the time-step size on the accuracy of the predictions are studied.

The flow around an airfoil at an angle of attack of 30° is taken as a test case at a high Reynolds number of 1.83×10^6.

2. GOVERNING EQUATIONS

The three laws governing the fluid motion are for the conservation of mass, momentum and energy. Here, the density and the temperature are assumed constant and the energy equation can be ignored. The continuity equation in a conservation form becomes

$$\int_S \rho \mathbf{V} \cdot \mathrm{d}\mathbf{S} = 0 \tag{1}$$

where ρ is the density and $\mathbf{V} = u\mathbf{i} + v\mathbf{j}$ is the velocity of the fluid. Integration is taken over the control volume faces. This constraint simply states that at every moment the mass flow out from the control volume equals the mass flow in. The momentum equation in the x-direction is written as

$$\frac{\partial}{\partial t} \int_V \rho u \, \mathrm{d}V + \int_S \rho u \mathbf{V} \cdot \mathbf{n} \, \mathrm{d}S + \int_S p n_x \, \mathrm{d}S - \mu \int_S \left(n_x \frac{\partial u}{\partial x} + n_y \frac{\partial u}{\partial y} \right) \mathrm{d}S = 0 \tag{2}$$

Above, p is the pressure and $\mathbf{n}=n_x\mathbf{i}+n_y\mathbf{j}$ is a unit normal of the control volume face. Body forces are ignored. The equation in the y-direction is obtained by replacing the velocity component u with v and the wall-normal component n_x in the pressure term with n_y.

3. SOLVER FOR STEADY FLOWS

3.1. Momentum equations

Cartesian equations are solved sequentially; first in the x-direction and then in the y-direction. Within both Cartesian directions, a contribution from both curvilinear i- and j-direction of the grid is computed. An implicit Euler method is used in solving Equation (2), which, after discretization for a node (ij) becomes

$$V_{ij}\left(\frac{\rho u^{n+1}-\rho u^n}{\Delta t}\right)_{ij}=-\sum_{\phi=1}^{\text{faces}}(\hat{F}_\phi^{\text{inv}}-\hat{F}_\phi^{\text{visc}})^{n+1}S_\phi \tag{3}$$

where the inviscid flux in the x-direction at the cell face ϕ is

$$F_\phi^{\text{inv}}=\hat{F}_\phi^{\text{inv}}S_\phi=S_\phi\rho u_\phi\mathbf{V}_\phi\cdot\mathbf{n}_\phi+(Sn_x p)_\phi=\dot{m}_\phi u_\phi+(Sn_x p)_\phi \tag{4}$$

Here, $\dot{m}_\phi=S_\phi\rho\mathbf{V}_\phi\cdot\mathbf{n}_\phi$ is a mass flow through the face ϕ. At the face $(i+\frac{1}{2},j)$ (i.e. in the i-direction), the viscous flux for the u-momentum equation becomes

$$F_{i+1/2,j}^{\text{visc}}=\frac{S\mu}{\Delta\xi}(u_{i+1,j}-u_{ij}) \tag{5}$$

where $\Delta\xi$ is the distance between the nodes (ij) and $(i+1,j)$. Here, a thin-shear-layer approximation is used in each co-ordinate direction instead of calculating the derivatives by using the generalized divergence theorem of Gauss. In a Cartesian grid both approximations are the same.

In the implicit solution, the flux is linearized by using a first-order upwind discretization as

$$\begin{aligned}
&F_{i+1/2,j}^{n+1}(u_{ij},u_{i+1,j},p_{i+1/2,j})\\
&\quad=F_{i+1/2,j}^{n}+\frac{\partial F_{i+1/2,j}^{n}}{\partial t}\Delta t\\
&\quad=F_{i+1/2,j}^{n}+\frac{\partial F_{i+1/2,j}^{n}}{\partial u_{ij}}\Delta u_{ij}+\frac{\partial F_{i+1/2,j}^{n}}{\partial u_{i+1,j}}\Delta u_{i+1,j}+\frac{\partial F_{i-1/2,j}^{n}}{\partial p_{i+1/2,j}}\Delta p_{i-1/2,j}\\
&\quad=F_{i+1/2,j}^{n}(u_{ij},u_{i+1,j},p_{i+1/2,j})+\left(\max(\dot{m}_{i+1/2,j},0)+\left(\frac{\mu_{i+1/2}}{\Delta\xi}\right)\right)\Delta u_{ij}\\
&\qquad-\left(\max(-\dot{m}_{i+1/2,j},0)+\left(\frac{\mu_{i+1/2}}{\Delta\xi}\right)\right)\Delta u_{i+1,j}+Sn_{x_{i+1/2,j}}\Delta p_{i+1/2,j}
\end{aligned} \tag{6}$$

where $\Delta u_{ij}=u_{ij}^{n+1}-u_{ij}^n$ and $\Delta p_{ij}=p_{ij}^{n+1}-p_{ij}^n$. Above, the index $(i+\frac{1}{2},j)$ refers to the wall between nodes (ij) and $(i+1,j)$. The mass flow $m_{i+1/2,j}$ is computed as an average between

the nodes and it is kept constant in the linearization. The reader is reminded that the order of accuracy is not limited by the linearization, but it is determined by the accuracy to which the solution is iterated.

In Equation (6), the normal of the wall **n** points into the direction of the increasing index i and j. After integration at every cell face, Equation (3) becomes

$$\left(\frac{V\rho}{\Delta t}\right)_{ij}\Delta u_{ij}=F^{n+1}_{i-1/2,j}+F^{n+1}_{i,j-1/2}-F^{n+1}_{i-1/2,j}-F^{n+1}_{i,j-1/2} \tag{7}$$

Linearized terms of Equation (6) are inserted into Equation (7). The diagonal coefficient of Δu_{ij} can be written by using the non-diagonal ones and the identity

$$\max(x,0)+\max(-y,0)=\max(-x,0)+\max(y,0)+(x-y) \tag{8}$$

Thus, the diagonal coefficient becomes

$$\begin{aligned}A_{P,ij}=&\left(\frac{V\rho}{\Delta t}\right)_{ij}-(A_W+A_E+A_S+A_N)_{ij}\\&-(\dot m_{i+1/2,j}-\dot m_{i-1/2,j}+\dot m_{i,j+1/2}-\dot m_{i,j-1/2})\end{aligned} \tag{9}$$

The last four terms in Equation (9), i.e. the mass residual, are ignored, which is well justified because in convergence it equals zero. The diagonal coefficient is thus always a sum of the non-diagonal ones with an opposite sign and the term from the time derivative, which also prevents a singularity. Other coefficients in Equation (9) are

$$\begin{aligned}A_{W,ij}&=-\left(\max(\dot m_{i-1/2,j},0)+\frac{\mu_{i-1/2,j}}{\Delta\xi}\right)\\A_{E,ij}&=-\left(\max(-\dot m_{i+1/2,j},0)+\frac{\mu_{i+1/2,j}}{\Delta\xi}\right)\\A_{S,ij}&=-\left(\max(\dot m_{i,j-1/2},0)+\frac{\mu_{i,j-1/2}}{\Delta\eta}\right)\\A_{N,ij}&=-\left(\max(-\dot m_{i,j+1/2},0)+\frac{\mu_{i,j+1/2}}{\Delta\eta}\right)\end{aligned} \tag{10}$$

Equation (3) can now be written for the node (ij)

$$\begin{aligned}&A_{P,ij}\Delta u_{ij}+A_{W,ij}\Delta u_{i-1,j}+A_{E,ij}\Delta u_{i+1,j}+A_{S,ij}\Delta u_{i,j-1}+A_{N,ij}\Delta u_{i,j+1}\\&\quad=-\sum_{\phi=1}^{\text{faces}}(Sn_x)_\phi\Delta p_\phi+F^n_{i-1/2,j}+F^n_{i,j-1/2}-F^n_{i+1/2,j}-F^n_{i,j+1/2}\end{aligned} \tag{11}$$

The first term on the right-hand side of Equation (11) includes the pressure at the time level $n+1$ and in an iterative solution the whole term is ignored. This simplification also follows if the fluxes are linearized with respect to the velocities only.

3.2. Pressure coupling

The solution of the momentum equation must be coupled with pressure. The connection is the pressure correction equation, which is derived next. The last four terms of Equation (11) cancel when the steady state is reached. The linearized increments Δu and Δp are replaced in the following by iterative corrections u' and p':

$$A_{P,ij}u'_{ij} + A_{W,ij}u'_{i-1,j} + A_{E,ij}u'_{i+1,j} + A_{S,ij}u'_{i,j-1} + A_{N,ij}u'_{i,j+1} = -\sum_{\phi=1}^{\text{faces}} S_\phi n_{\phi x} p'_\phi \tag{12}$$

where the standard simplification utilized in a SIMPLE method is to drop the non-diagonal terms from Equation (12) to derive a manageable equation. A discussion of this simplification can be found, for instance, in the classical book of Patankar [5]. The derivation above can be done in a shifted control volume to obtain u' at the cell face.

$$A_{P,i+1/2,j}u'_{i+1/2,j} = -(Sn_x p')_{i+1,j} + (Sn_x p')_{ij} - (Sn_x p')_{i+1/2,j+1/2} + (Sn_x p')_{i+1/2,j-1/2} \tag{13}$$

Since the linearization was done with respect to the convective velocities, the coefficients $A_{P,\phi}$ are similar for all other Cartesian components of the same cell face ϕ. Equation (13) can be written for v' by replacing the cell face-normal n_x with n_y. The continuity equation states that

$$\begin{gathered}\sum_{\phi=1}^{\text{faces}_{ij}} (\rho(\mathbf{V}^* + \mathbf{V}') \cdot \mathbf{n}S)_\phi = 0 \\ \sum_{\phi=1}^{\text{faces}_{ij}} (u' n_x S)_\phi + (v' n_y S)_\phi = -\sum_{\phi=1}^{\text{faces}_{ij}} (\rho \mathbf{V}^* \cdot \mathbf{n}S)_\phi\end{gathered} \tag{14}$$

where $\mathbf{V}^*$ is the velocity field that does not obey the mass balance and $\mathbf{V}'$ is the iterative correction. Next, we assume that the grid is nearly orthogonal, which is a reasonable approximation of a good-quality grid. Then, in Equation (13) the normals in the cardinal directions $(n_x)_{ij}$ and $(n_x)_{i+1,j}$ are nearly orthogonal to those with half-integer subscripts. Thus, after having inserted u' and v' from Equation (13) into Equation (14), the following equation is obtained:

$$\begin{aligned}&\frac{1}{A_{P,i+1/2,j}}[-(S^2 p')_{i+1,j} + (S^2 p')_{ij}] + \frac{1}{A_{P,i,j+1/2}}[-(S^2 p')_{i,j+1} + (S^2 p')_{ij}] \\ &+ \frac{1}{A_{P,i-1/2,j}}[-(S^2 p')_{i-1,j} + (S^2 p')_{ij}] + \frac{1}{A_{P,i,j-1/2}}[-(S^2 p')_{i,j-1} + (S^2 p')_{ij}] \\ &= -\Delta \dot{m}_{ij}\end{aligned} \tag{15}$$

where the mass balance $-\Delta \dot{m}_{ij}$ is the right-hand side of Equation (14). The surface areas S are approximated as averages and after some re-grouping of the terms we finally obtain the pressure correction equation

$$B_{P,ij}p'_{ij} + B_{W,ij}p'_{i-1,j} + B_{E,ij}p'_{i+1,j} + B_{S,ij}p'_{i,j-1} + B_{N,ij}p'_{i,j+1} = -\Delta \dot{m}_{ij} \tag{16}$$

where the coefficients are defined as

$$B_{W,ij} = \frac{S^2_{i-1/2,j}}{A_{P,i-1/2,j}}, \quad B_{E,ij} = \frac{S^2_{i+1/2,j}}{A_{P,i+1/2,j}}$$

$$B_{S,ij} = \frac{S^2_{i,j-1/2}}{A_{P,i,j-1/2}}, \quad B_{N,ij} = \frac{S^2_{i,j+1/2}}{A_{P,i,j+1/2}} \tag{17}$$

$$B_{P,ij} = \frac{S^2_{i,j-1/2}}{A_{P,ij}}$$

3.3. Calculation of cell-face velocities

In a co-located, orthogonal grid, the velocity does not depend on the pressure at the same node (ij), which can lead to a non-physical converged solution, a phenomenon known as a checkerboard solution. This is the reason why methods have been developed to couple the pressure and the velocity in the calculation of mass balance. Rhie and Chow [6] have presented a remedy for uncoupling, which is in wide use. This remedy is applied in the SIMPLE solver. In a calculation of mass balance, the cell-face velocities are computed as

$$\bar{u}_{i-1/2,j} = \frac{1}{2}(\bar{u}_{i-1,j} + \bar{u}_{ijk}) + C\frac{S_{i-1/2,j}}{4A_{P,i-1/2,j}}[p_{i-2,j} - 3p_{i-1,j} + 3p_{ij} - p_{i-1,j}] \tag{18}$$

The pressure term in Equation (18) adds numerical dissipation and it is similar to the artificial viscosity term presented by Jameson [1]. In a smooth pressure field, the term will become negligible. The pressure term is multiplied by a constant C in the range 0.01–0.5 to adjust an optimum coupling [7]. In this study, a value of 0.5 for the constant is set.

3.4. Calculation of time step

A local time stepping is applied in the SIMPLE steady-state solver. In each cell, the local time step $\Delta\Theta_{ij}$ is defined as

$$\Delta\Theta_{ij} = \min\left\{\frac{\mathrm{CFL}V_{ij}}{|\mathbf{V}_{ij}\cdot\mathbf{S}^i_{ij}| + |\mathbf{V}_{ij}\cdot\mathbf{S}^j_{ij}|}, \frac{C_{\mathrm{DIFF}}2V^2_{ij}}{\nu|\mathbf{S}^i_{ij}|}, \frac{C_{\mathrm{DIFF}}2V^2_{ij}}{\nu|\mathbf{S}^j_{ij}|}\right\} \tag{19}$$

where $\mathbf{S}^i_{ij} = \frac{1}{2}(\mathbf{S}_{i-1/2,j} + \mathbf{S}_{i+1/2,j})$ and other surfaces are defined in the same manner. The first term comes from convection and the two last terms are due to diffusion. CFL and C_{DIFF} are parameters given by the user to control the size of the step.

3.5. Solution sequence

A flow chart of the solver is presented in Figure 1. The momentum equations (11) are solved in series with a multigrid (MG) solver. The mass balance is calculated with face velocities (18) that are coupled with the pressure. The mass flux error is used as a source in the pressure correction equation (16), which is solved with a multigrid solver.

The MG algorithm solves the problem at the dense level first and moves the residual to the next coarsest level as a source. The coarse grid problem is approximated from the finer one.

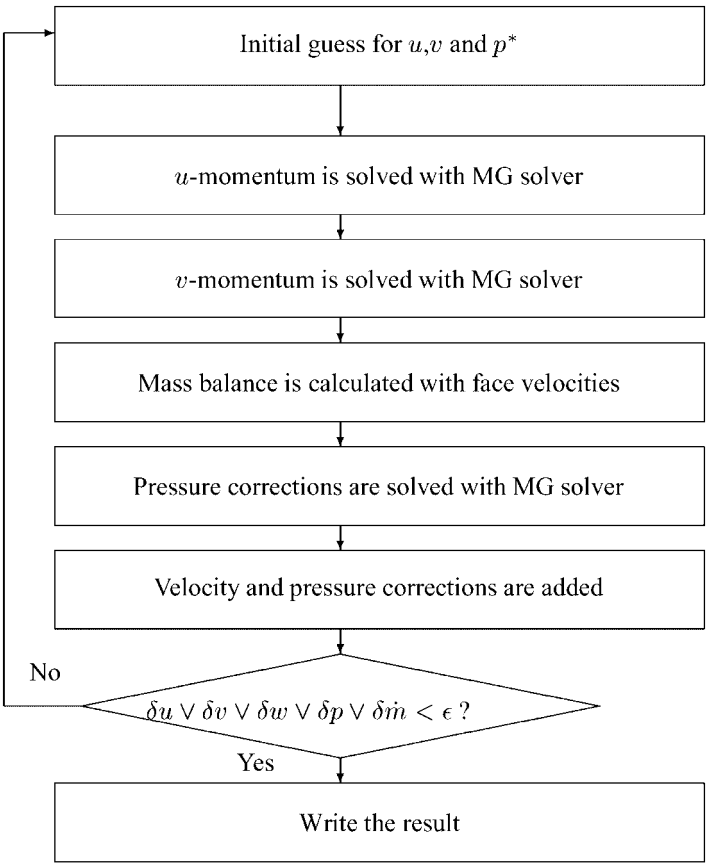

Figure 1. Flow chart of the SIMPLE solution.

The process is called a Galerkin coarse-grid approximation (GCA). After the coarsest grid level, the corrections are added to the unknown of each finer level, or the problem can be iterated also on the way up. The line Gauss Seidel (LGS) method is used at each level as a smoother, Reference [7] and Pensala (unpublished memorandum '3-D multigrid solver for Poisson-type equations' (in Finnish). HUT, 1996) give a detailed description of the MG solver. The pressure corrections p' and the velocity corrections from Equation (13) are added to the pressures and the velocities multiplied by the underrelaxation coefficients α_{p} and α_{u}

$$\begin{aligned} u^{n+1} &= u^* + \alpha_{\mathrm{u}} u' \\ p^{n+1} &= p^* + \alpha_{\mathrm{p}} p' \end{aligned} \tag{20}$$

Depending on the case, α_{p} usually varies from 0.1 to 0.8. In order for the velocities to satisfy the continuity equation, α_{u} should be 1 at this stage. The iteration cycle is repeated until the convergence criterion is satisfied. The criterion can be set in many different ways and it

can depend on any primary variable or the balance of mass fluxes. Usually, an L_2-norm of a residual of some variable must converge below a preset limit.

4. SOLVERS FOR UNSTEADY FLOWS

4.1. Explicit Euler scheme

The momentum equations are solved in series: first in the x-direction and then in the y-direction. Within each Cartesian direction, a contribution from both the curvilinear i- and j-direction of the grid is computed. Equation (2) for the x-momentum is discretized with an explicit Euler scheme for a node ij

$$\rho u_{ij}^{n+1} = \rho u_{ij}^{n} - \frac{\Delta t}{V_{ij}} \sum_{\text{faces}} (f_x^{\text{conv}} S - f_x^{\text{visc}} S)^n - \frac{\Delta t}{V_{ij}} \sum_{\text{faces}} (p n_x S)^n \tag{21}$$

where $f_x^{\text{conv}} S$ and $f_x^{\text{visc}} S$ are the convective and the viscous fluxes in the x-direction at the cell faces. The spatial treatment of these fluxes is of no importance here. With Equation (21), the solution can be advanced from time step n to time step $n+1$. Pressure is determined from a mass-balance equation. In order to derive that, Equation (21) is written for staggered volumes around the cell (ij), as shown in Figure 2. At the time step $n+1$, the mass conservation is enforced

$$\sum_{\text{faces}} (\rho \mathbf{V} \cdot \mathbf{S})^{n+1} = \sum_{\text{faces}} (\rho \mathbf{V} \cdot \mathbf{S})^{n} + \frac{\Delta t}{V_{ij}} \sum_{\text{faces}} (\mathbf{R} \cdot \mathbf{S})^n - \frac{\Delta t}{V_{ij}} \sum_{\text{faces}} (p \mathbf{S}' \cdot \mathbf{S})^n = 0 \tag{22}$$

where $\mathbf{S}'$ refers to a staggered surface and the residual

$$\mathbf{R} = R_x \mathbf{i} + R_y \mathbf{j} = -\sum_{\text{faces}'} [(f_x^{\text{conv}} S - f_x^{\text{visc}} S)\mathbf{i} + (f_y^{\text{conv}} S - f_y^{\text{visc}} S)\mathbf{j}] \tag{23}$$

is computed in staggered cells surrounding the control volume. The staggered grid is shown in Figure 2.

$$\begin{aligned}
&\sum_{\text{faces}} (p \mathbf{S}' \cdot \mathbf{S}) \\
&= \sum_{\alpha = x,y} \Delta t \times \left\{ \left(\frac{S n_\alpha}{V} \right)_{i+1/2,j} [(S n_\alpha p)_{i+1,j} - (S n_\alpha p)_{i,j} + (S n_\alpha p)_{i+1/2,j+1/2} - (S n_\alpha p)_{i+1/2,j-1/2}] \right. \\
&\quad + \left(\frac{S n_\alpha}{V} \right)_{i,j+1/2} [(S n_\alpha p)_{i,j+1} - (S n_\alpha p)_{i,j} + (S n_\alpha p)_{i+1/2,j+1/2} - (S n_\alpha p)_{i-1/2,j+1/2}] \\
&\quad + \left(\frac{S n_\alpha}{V} \right)_{i-1/2,j} [(S n_\alpha p)_{i,j} - (S n_\alpha p)_{i-1,j} + (S n_\alpha p)_{i-1/2,j-1/2} - (S n_\alpha p)_{i-1/2,j-1/2}] \\
&\quad \left. + \left(\frac{S n_\alpha}{V} \right)_{i+1/2,j} [(S n_\alpha p)_{i,j} - (S n_\alpha p)_{i,j-1} + (S n_\alpha p)_{i+1/2,j-1/2} - (S n_\alpha p)_{i-1/2,j-1/2}] \right\}
\end{aligned} \tag{24}$$

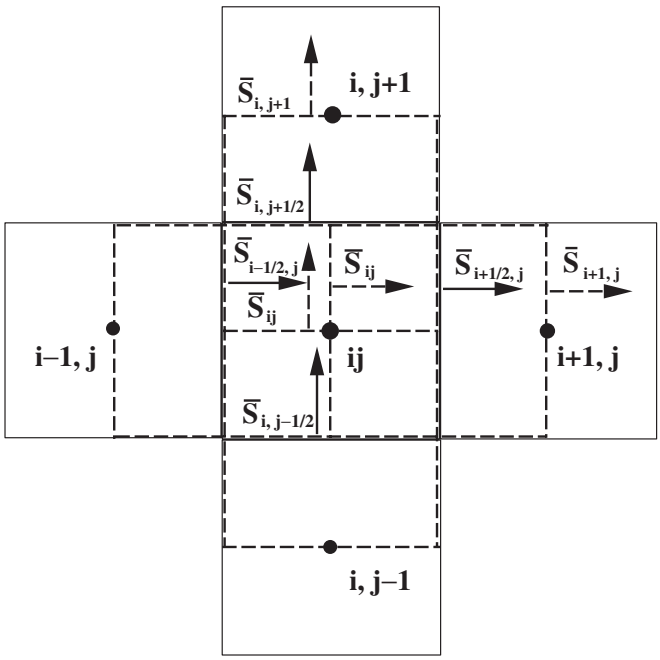

Figure 2. Staggered grid around the control volume ij shown in two dimensions. Here, $\mathbf{S}$ is the surface vector, which points in the direction of growing index i or j. Dotted surfaces and their vector arrows belong to the staggered grid.

As with SIMPLE, the pressure term is approximated by considering only the cardinal directions of the pressure differences. Thus, the last two terms in each line of Equation (24) are ignored. In addition, the staggered surfaces are approximated as the corresponding surface between them in the control volume. After some re-grouping of the terms and insertion back into Equation (22), we obtain the Poisson equation for the pressure

$$\begin{aligned} &A_{W,ij}\,p_{i-1,j} + A_{E,ij}\,p_{i+1,j} + A_{S,ij}\,p_{i,j-1} + A_{N,ij}\,p_{i,j-1}A_{P,ij}\,p_{ij} \\ &\quad = \sum_{\text{faces}} (\rho \mathbf{V}\cdot\mathbf{S})^n + \sum_{\text{faces}} (\mathbf{R}\cdot\mathbf{S})^n \end{aligned} \tag{25}$$

where the coefficients are

$$\begin{aligned} A_{W,ij} &= \frac{\Delta t S_{i-1/2,j}^2}{V_{i-1/2,j}}, \qquad A_{E,ij} = \frac{\Delta t S_{i+1/2,j}^2}{V_{i+1/2,j}} \\ A_{S,ij} &= \frac{\Delta t S_{i,j-1/2}^2}{V_{i,j-1/2}}, \qquad A_{N,ij} = \frac{\Delta t S_{i,j+1/2}^2}{V_{i,j+1/2}} \\ A_{P,ij} &= -(A_{W,ij} + A_{E,ij} + A_{S,ij} + A_{N,ij}) \end{aligned} \tag{26}$$

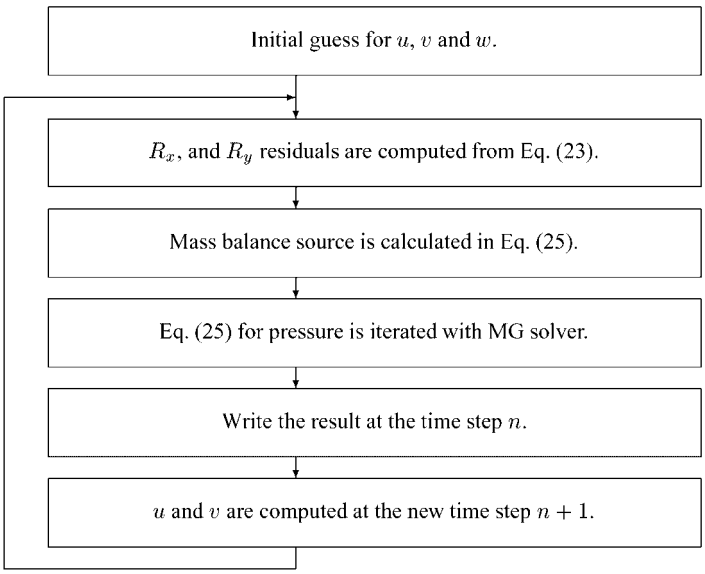

Figure 3. Flow chart of the explicit Euler solution.

In Equation (25), the first term on the right-hand side is the mass balance from the present time step n, which should be zero. This term can be retained with consideration that, with an iterative method, the equation has not necessarily converged completely.

The solution sequence of the explicit Euler scheme is shown in Figure 3. The computation is started with an initial guess. The residuals from the convective and viscous terms are computed from Equation (23) and the right-hand side source of Equation (25) is formed with the present mass balance included. The Poisson equation is iterated for pressures with a MG solver to a preset convergence limit. Now the time step n is completed and the result can be written. Next, the new velocities at the time step $n+1$ are computed from the momentum equations. The order of computation of the velocities and the pressure at a given time step is different from the implicit SIMPLE. In fact, in the explicit Euler scheme, the velocities at every stage of the solution obey the mass balance.

4.2. *Fractional-step Adams–Bashford scheme*

Consider again Equations (2) with convection and diffusion terms discretized in the following second-order accurate Adams–Bashford [8] scheme with respect to time. The pressure is discretized with a first-order accurate Euler scheme:

$$\rho \mathbf{V}_{ij}^{n+1} = \rho \mathbf{V}_{ij}^{n} + \frac{\Delta t}{2V_{ij}} (3\mathbf{R}_{ij}^{n} - \mathbf{R}_{ij}^{n-1}) - \frac{\Delta t}{V_{ij}} \sum_{\text{faces}} (p\mathbf{S})^{n-1} \tag{27}$$

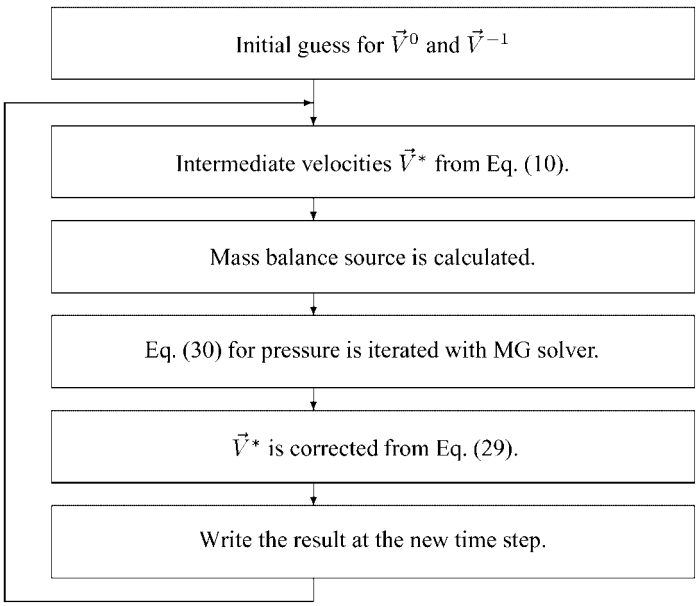

Figure 4. Flow chart of the Adams–Bashford solution.

where $\mathbf{R}_{ij}$ is defined by Equation (23), although the sum is taken at the faces around the control volume ij. To compute Equation (27) a fractional-step approach is applied [4, 9]:

$$\rho \mathbf{V}_{ij}^* = \rho \mathbf{V}_{ij}^n + \frac{\Delta t}{2V_{ij}} (3\mathbf{R}_{ij}^n - \mathbf{R}_{ij}^{n-1}) \tag{28}$$

$$\rho \mathbf{V}_{ij}^{n+1} = \rho \mathbf{V}_{ij}^* - \frac{\Delta t}{V_{ij}} \sum_{\text{faces}} (p\mathbf{S})^{n+1} \tag{29}$$

For the latter equations, the mass balance is required for the control volume V_{ij} at the time step $n+1$. Again a Poisson equation for the pressure is obtained

$$A_{W,ij}\, p_{i-1,j} + A_{E,ij}\, p_{i+1,j} + A_{S,ij}\, p_{i,j-1} + A_{N,ij}\, p_{i,j-1} + A_{P,ij}\, p_{ij} = \sum_{\text{faces}} (\rho \mathbf{V}^* \cdot \mathbf{S}) \tag{30}$$

where the coefficients are the same as with the Euler scheme in Equation (26).

The solution sequence of the Adams–Bashford scheme is shown in Figure 4. The computation is started with an initial guess, which is used for both previous steps. The intermediate velocities $\mathbf{V}^*$ are computed and interpolated to the cell faces to calculate the mass balance. The Poisson equation (30) is iterated for the pressures with a MG solver to a preset convergence limit. Finally, the new velocities can be corrected from Equation (29) to obtain the result at the new time step.

4.3. Three-level implicit scheme based on SIMPLE

The implicit SIMPLE method presented earlier can be turned into a time-accurate method. Let us consider the following generic multistep method:

$$(1+\gamma)(\rho\mathbf{V})^{n+1} - (1+2\gamma)(\rho\mathbf{V})^{n} + \gamma(\rho\mathbf{V})^{n-1} = \frac{\Delta t}{V_{ij}}[(1-\beta)\mathbf{R}^{n} + \beta\mathbf{R}^{n-1}] \tag{31}$$

where residual $\mathbf{R}$ includes the inviscid, the viscous and the pressure terms. With different choices of parameters β and γ, the following time advancement schemes can be realized, with $\beta=\gamma=0$ the explicit Euler, with $\beta=1,\ \gamma=0$ an implicit Euler, with $\beta=0.5,\ \gamma=0$ a Crank–Nicolson and with $\beta=1.0, \gamma=0.5$ a three-level implicit (3-LI) scheme. The last two methods are second-order accurate. Equation (31) is linearized at the state k between the solved state n and the state $n+1$ to be computed:

$$(1+\gamma)[\rho(\mathbf{V}^{k}+\mathbf{V}^{n+1}-\mathbf{V}^{k})] - (1+2\gamma)\rho\mathbf{V}^{n} + \gamma\rho\mathbf{V}^{n-1} = \frac{\Delta t}{V_{ij}}\left[(1-\beta)\mathbf{R}^{n} + \beta\left(\mathbf{R}^{k} + \left[\frac{\partial\mathbf{R}}{\partial\rho\mathbf{V}}\right]^{k}\rho(\mathbf{V}^{n+1}-\mathbf{V}^{k})\right)\right] \tag{32}$$

Let us write $\Delta\mathbf{V}=\mathbf{V}^{n+1}-\mathbf{V}^{k}$ and re-group the terms as follows:

$$\left(1+\gamma-\beta\frac{\Delta t}{V_{ij}}\left[\frac{\partial\mathbf{R}}{\partial\rho\mathbf{V}}\right]^{k}\right)\rho\Delta\mathbf{V} = \rho(-(1+\gamma)\mathbf{V}^{k} + (1+2\gamma)\mathbf{V}^{n} - \gamma\mathbf{V}^{n-1}) + \frac{\Delta t}{V_{ij}}[(1-\beta)\mathbf{R}^{n} + \beta\mathbf{R}^{k}] \tag{33}$$

From Equation (33), $\mathbf{V}^{n+1}$ can be iterated, but it must be stabilized for arbitrary time steps. This can be done by replacing γ on the diagonal by $\Delta t/\Delta\Theta$ where $\Delta\Theta$ is the local pseudo-time step of the steady-state solver [10]. If the real-time step grows or the local pseudo-time step gets smaller then the diagonal element grows, which stabilizes the equation. After this, Equation (33) is multiplied by the factor $\Delta\Theta/(\Delta t+\Delta\Theta)$ and the following form is obtained:

$$\left(1-\frac{\Delta t\Delta\Theta}{\Delta t+\Delta\Theta}\frac{\beta}{V_{ij}}\left[\frac{\partial\mathbf{R}}{\partial\rho\mathbf{V}}\right]^{k}\right)\rho\Delta\mathbf{V} = \frac{\Delta t\Delta\Theta}{\Delta t+\Delta\Theta}\left\{\rho\left(\frac{-(1+\gamma)\mathbf{V}^{k}+(1+2\gamma)\mathbf{V}^{n}-\gamma\mathbf{V}^{n-1}}{\Delta t}\right) + \frac{1}{V_{ij}}[(1-\beta)\mathbf{R}^{n}+\beta\mathbf{R}^{k}]\right\} \tag{34}$$

Equation (34) can be written in a more compact form by considering $\Delta t\Delta\Theta/(\Delta t - \Delta\Theta)$ as a modified time step Δt_{mod} and the right-hand side as a modified residual $\mathbf{R}_{\mathrm{mod}}$.

$$\left(1 - \frac{\beta\Delta t_{\mathrm{mod}}}{V_{ij}}\left[\frac{\partial \mathbf{R}}{\partial \rho \mathbf{V}}\right]^k\right)\rho\Delta\mathbf{V} = \frac{\Delta t_{\mathrm{mod}}}{V_{ij}}\mathbf{R}_{\mathrm{mod}}^k \tag{35}$$

The solution algorithm of Equation (34) is shown in Figure 5. The computation is started with an initial guess, which is also copied at the previous time levels. The momentum equations are solved sequentially with the MG solver. The mass balance is computed and used as a source for the pressure correction equation, which is solved with the MG solver. If the residual of u, v and p or mass balance is greater than some preset convergence criteria, the solution is iterated within the time step. As the convergence is reached, the result is written and the iteration of the solution of the new time level is started by updating the variables at the old and present time levels.

4.4. Time-step determination

In the implicit SIMPLE method, Equation (19) is employed to compute the local time step Δt in each cell. To stabilize the computation, a modified local step $\Delta t_{\mathrm{mod}} = \Delta t\Delta\Theta/(\Delta t + \Delta\Theta)$ is used. The real-time step Δt is given by the user. In explicit schemes everywhere in the computational area, the same real-time step, which is the smallest of the local steps, is computed from a similar criterion as Equation (19)

$$\begin{aligned}\Delta t &= \min_{ij}\left[\Delta t_{ij}\right] \\ &= \min_{ij}\left[\min\left\{\frac{\mathrm{CFL}V_{ij}}{|\mathbf{V}_{ij}\cdot\mathbf{S}_{ij}^i|}, \frac{\mathrm{CFL}V_{ij}}{|\mathbf{V}_{ij}\cdot\mathbf{S}_{ij}^j|}, \frac{C_{\mathrm{DIFF}}2V_{ij}^2}{\nu|\mathbf{S}_{ijk}^i|}, \frac{C_{\mathrm{DIFF}}2V_{ij}^2}{\nu|\mathbf{S}_{ij}^j|}\right\}\right]\end{aligned} \tag{36}$$

where $\mathbf{S}_{ij}^i$ is defined as in Equation (19). In Equation (36), the convective and diffusive steps are computed separately in all the co-ordinate directions.

5. STEADY FLOW OVER A CYLINDER

5.1. Test case

The two-dimensional steady-state solver is tested in the case of a flow past a cylinder. The Reynolds number based on the cylinder diameter D:

$$Re_D = \frac{U_\infty D}{\nu} \tag{37}$$

is 40, which means that the flow is stationary and two-dimensional. Here, U_∞ is the free-stream velocity. A second-order central discretization scheme is used for the convective and diffusive terms. The grid is of the O-type and the dimensions are $10.5D$ and 2π in the radial (j) and azimuthal (i) directions. The number of cells is 96×96. The minimum i-face is connected to the maximum i-face, so a periodic boundary condition is used in that direction.

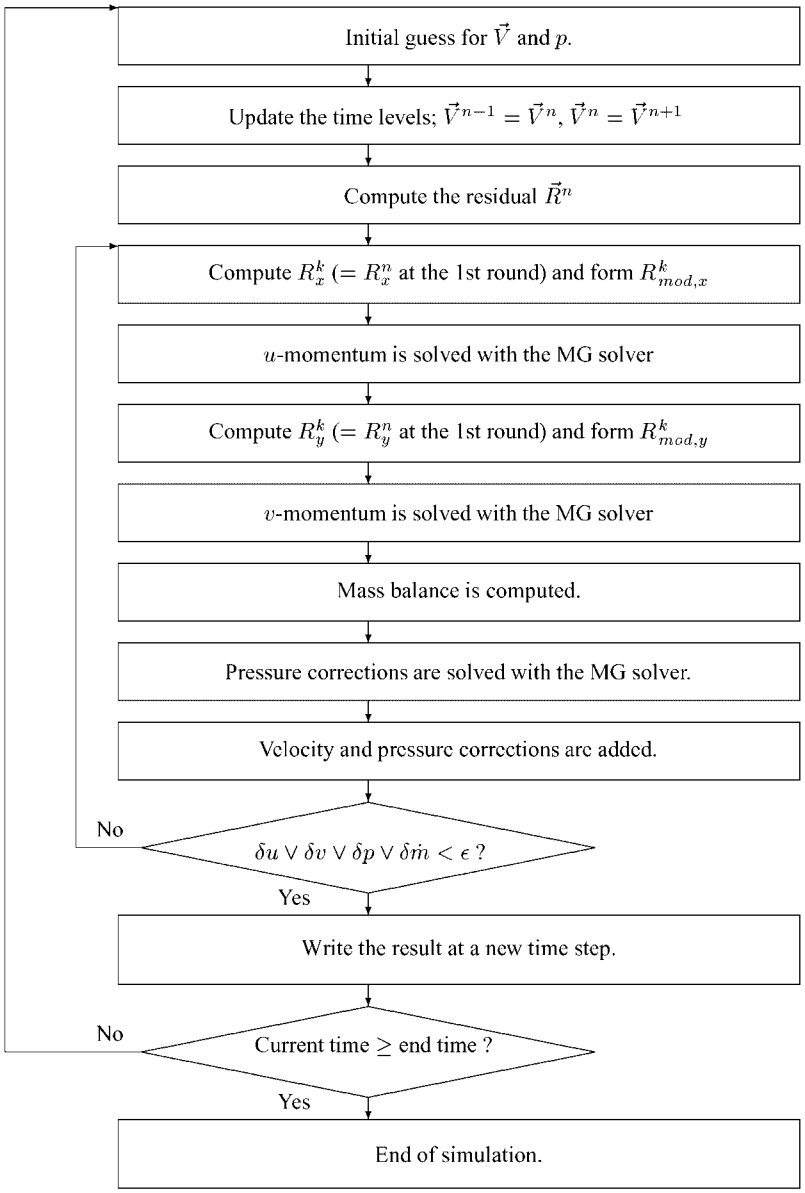

Figure 5. Flow chart of the SIMPLE-based 3-LI solution.

The velocities and the pressure are fixed in the ghost cells at the maximum j-boundary, which is called a Dirichlet condition. A no-slip condition is used at the minimum j-boundary, i.e. at the cylinder wall. A zero-gradient condition is set for the pressure in the wall-normal direction. At each iteration, one 1–1–1–5–5–0–0–0–0-cycle for the pressure and one 1–1–1–0–0-cycle

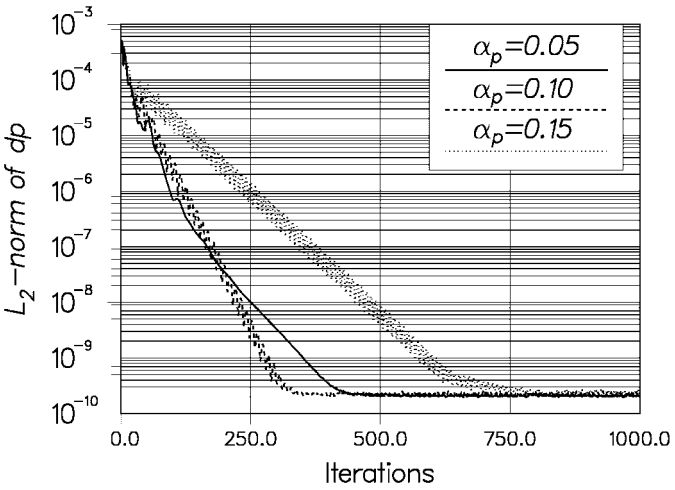

Figure 6. Convergence histories of the pressure corrections with different values of α_p.

for each momentum equation are iterated with the MG solver. The notation 1–1–1–5–5–0–0–0–0-cycle indicates that the problem is iterated or smoothed once on the three finest grid levels and five times on levels four and five. Four zeroes mean that corrections are transferred on the way up without smoothing. In the same manner, a notation of 1–1–1–0–0 indicates one iteration at three grid levels and the transfer of correction on the way up. The parameters CFL and C_{DIFF} are both set to be 2.

5.2. Results

The velocity vectors are shown behind the cylinder in Plate 1. The drag coefficient $C_{\mathrm{D}} = 1.5674$ and the reattachment length $2L/D = 4.2$ are in accordance with measurements and other simulations [11]. C_{D} is defined as $2F_{\mathrm{D}}/(\rho U_{\infty}^2 D)$, where F_{D} is the force acting on the cylinder in the external flow direction. The underrelaxation parameter α_{p} for the pressure had to be quite low. In Figure 6, the convergence histories of the pressure corrections with different values of α_{p} are shown. The best convergence is achieved as $\alpha_{\mathrm{p}} = 0.1$. Increasing the value to 0.2 causes divergence.

6. COMPARISON OF THE UNSTEADY METHODS

6.1. Test case 1

The test case 1 is a cylinder in a free stream. The case is computed with five different Reynolds numbers. 100, 200, 400, 800 and 1600, which means that all cases are time dependent. The grid is similar to the one in the steady-state computation and the same number of cells is used with each Reynolds number. The height of the first cell next to the cylinder surface is approximated to be around $y^+ = 1$ with all the Reynolds numbers. The stretching ratio varies from 1.02 to 1.06 between the grids. As in the steady-state case, the Dirichlet condition is

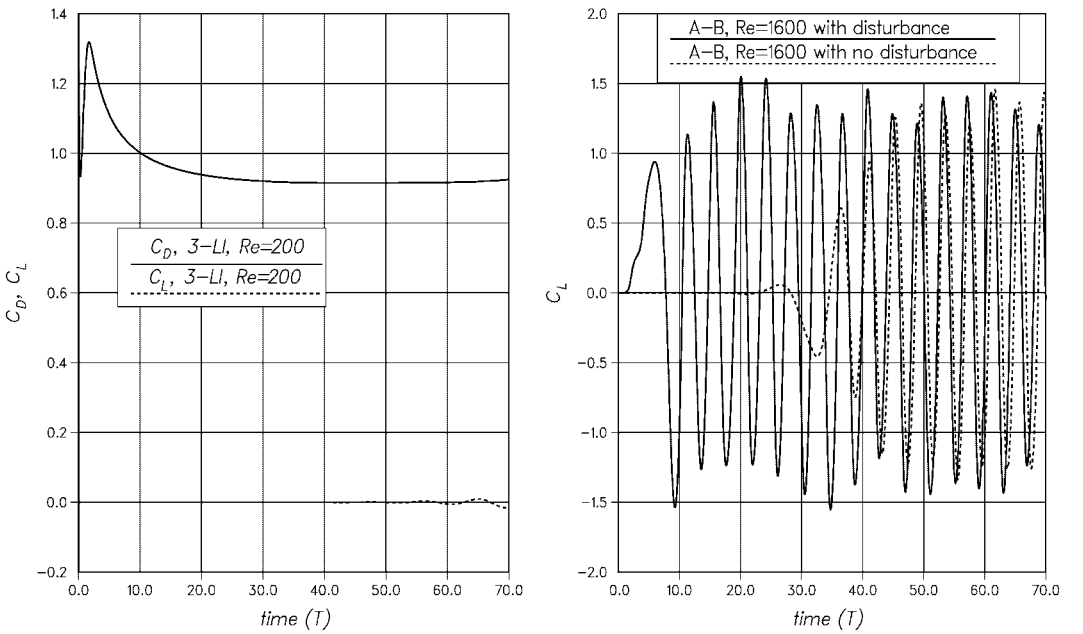

Figure 7. On the left, drag and lift coefficient curves from the simulation with the Reynolds number of 200 without the initial disturbance. The case has been computed with the three-level implicit scheme. On the right, the lift coefficient curves from two simulations, with and without the initial disturbance. The Reynolds number is 1600, and the method is Adams–Bashford.

used at the maximum j-boundary and a no-slip condition at the minimum j-boundary. At the cylinder wall, a zero gradient for the pressure in the wall normal direction is set. This Neumann condition requires a no-slip condition also for the intermediate velocities $\bar{V}^*$ (see e.g. Reference [9]). The second-order central discretization scheme is used for the convective and diffusive terms.

The simulation time of all the calculations is $70T$, where T stands for the time required for the free stream to travel the distance of the cylinder diameter D/U_∞. In the time interval $[T, 3T]$, an initial disturbance was given by rotating the cylinder clockwise according to the following surface velocity profile:

$$U_{\text{surf}} = 0.3U_\infty 4(t-T)(3T-t)/(2T)^2, \quad t \in [T, 3T] \tag{38}$$

Without any disturbance, all the simulations have to be run for a much longer time before numerical errors develop into a vortex-shedding flow. The case with the Reynolds number of 100 does not develop unsteadiness in the given time. With the Reynolds number of 200, some disturbance can be seen in the lift coefficient curve at the time $t \approx 60T$ in Figure 7, where also the lift coefficient curves from simulations with the Reynolds number of 1600 are plotted with and without the initial disturbance. Braza *et al.* [11] have found steady numerical solutions up to the Reynolds number of 1000.

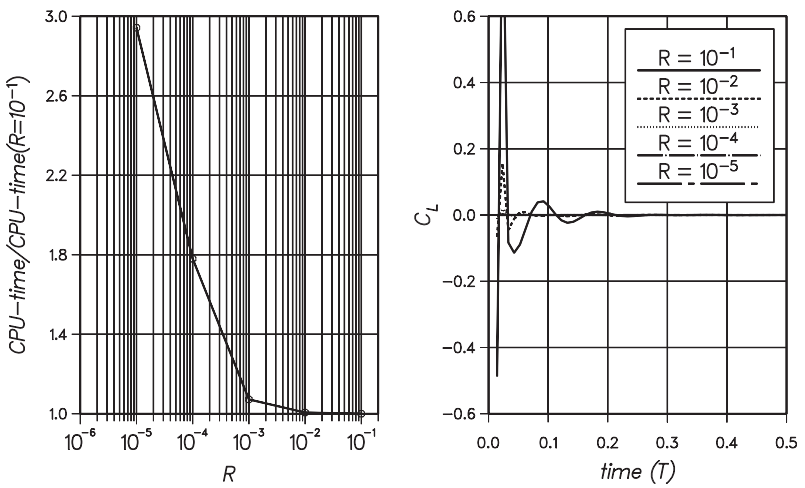

Figure 8. On the left, the normalized CPU times from the simulations with the Reynolds number of 100 and with different convergence limits. On the right, lift coefficient curves at the beginning of the computations. The method is Adams–Bashford.

6.2. *Parameters*

The sensitivity of the results to the convergence limit is studied next. The explicit methods advance the solution without any outer iterations and the only convergence criterion concerns the solution of the pressure equation. The Poisson equations (25) and (30) are iterated until the L^2-residual R of

$$R = \frac{\sqrt{(\mathbf{Ap} - \mathbf{b})^2}}{\sqrt{\mathbf{b}^2}} \tag{39}$$

is reduced below some preset limit at every time step. A test series was calculated with the Adams–Bashford method by varying R from 10^{-1} to 10^{-5} at the Reynolds number of 100. A maximum iteration number limit of 100 is set to prevent excessive iteration at the beginning of iteration. The MG cycle 1–1–1–1–1–0–0–0–0 is applied until the convergence criterion is reached. The results are evaluated in terms of the mean drag coefficient C_D and the lift coefficient C_L. C_L is defined as $2F_L/(\rho U_\infty^2 D)$, where F_L is the force acting on the cylinder upwards in the normal direction to that of the external flow. The simulation time is $70T$, where T is the normalized time D/U_∞.

It is a slight surprise that the flow is quite insensitive to the convergence criterion in this range. Only in the beginning of the computation are there some oscillations with low convergence limits, as seen in Figure 8. The cases with the two lowest convergence limits show no difference in CPU times, which means that, except in the beginning, one MG cycle is enough for convergence for both. After the tests, the convergence criterion for the Euler and the Adams–Bashford computation was set to be 10^{-3}, the same as that used by Davidson [12].

With the 3-LI scheme one 1–1–1–5–5–0–0–0–0-cycle for the pressure and one 1–1–1–0–0-cycle for the momentum equation with the MG solver are used. It appears that an accurate solution of these equations by running cycles more than once easily causes divergence. The

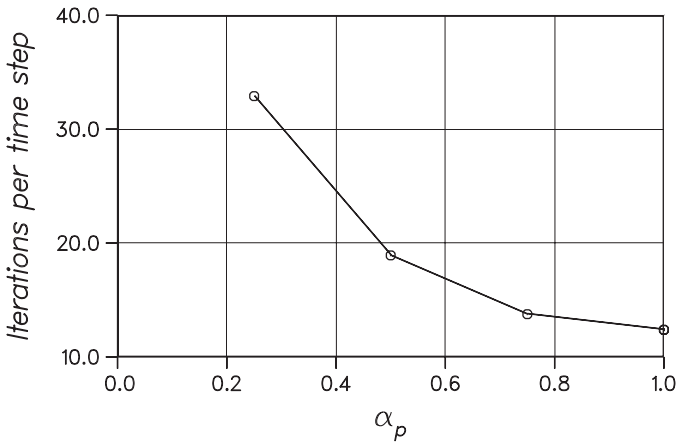

Figure 9. The number of subiterations as a function of the pressure correction underrelaxation. The Reynolds number is 100.

maximum subiteration number within the time step is set to be 100. Preliminary studies were undertaken to set the optimum values for the parameters. With the $Re=100$, it was observed that the underrelaxation of the pressure correction caused a slow convergence in time-accurate calculation. No underrelaxation at all ($\alpha_p = 1$) takes the lowest number of subiterations within the time step, which is shown in Figure 9. The CFL and C_{DIFF} parameters are both 2 and the real time-step length is $\Delta t=0.025T$ here. As the L_2-residual of the mass error normalized by the number of the cells is reduced to 10^{-9}, the iteration is stopped. With the CFL parameter values 1, 2 and 3, a shallow optimum is found at the value 2; the average numbers of subiterations per time step are 12.90, 12.11 and 12.95, respectively.

The effect of the convergence criterion on the lift coefficient curves is seen in Figure 10. The limits 10^{-9}, 10^{-8} and 10^{-7} of the L_2-residual of the mass error were tested. The simulation with the limit of 10^{-7} shows oscillations in the beginning of the computation and it deviates from the other two. The average convergence of various variables within the time step are found in Table I, where the quantities are defined as

$$\mathscr{H}(\phi)=\frac{L_2(\phi)_{\mathrm{end}}}{L_2(\phi)_{\mathrm{ini}}} \tag{40}$$

where $L_2(\phi)_{\mathrm{ini}}$ and $L_2(\phi)_{\mathrm{end}}$ are the L_2-norms of the variable ϕ from the first and the last iteration round, respectively. The quantity $\mathscr{R}$, estimates Equation (39) as

$$\mathscr{R}=\frac{\sqrt{(\mathbf{A}\mathbf{p}')^2}}{\sqrt{\mathbf{b}_{\mathrm{ini}}^2}} \tag{41}$$

where $\mathbf{b}_{\mathrm{ini}}$ is taken from the first iteration round in a time step. After these tests, a convergence limit of 10^{-9} for the mass error at the end of the time step was selected for the rest of the computations. In each computation, some test runs were performed in order to find optimal values for the pressure underrelaxation parameters. With the implicit schemes, the time-step

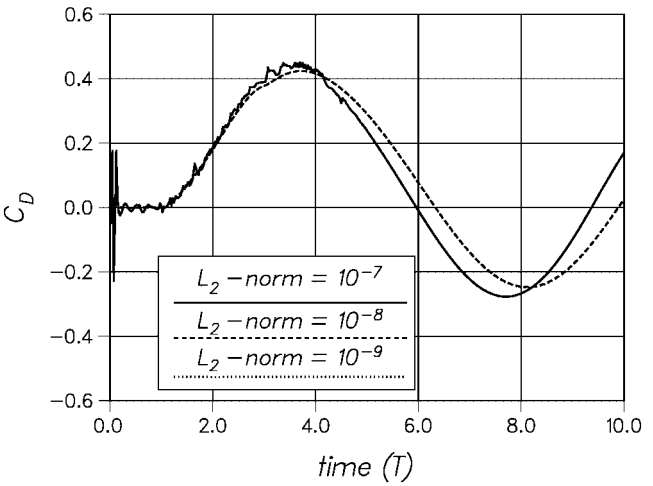

Figure 10. The lift coefficient curves from the simulations with different convergence limits of the mass error. The simulation with the limit 10^{-7} shows oscillations and deviates from the other two. The Reynolds number is 100.

Table I. The convergence test results with the Reynolds number of 100. See the text for the definition of the symbols in the table.

Convergence limit	Iterations per step	$\mathscr{H}(u)$	$\mathscr{H}(v)$	$\mathscr{H}(w)$	$\mathscr{R}$
10^{-7}	4.53	1.79×10^{-1}	2.10×10^{-1}	1.94×10^{-1}	1.01×10^{-1}
10^{-8}	7.77	3.58×10^{-2}	4.46×10^{-2}	2.79×10^{-2}	1.79×10^{-2}
10^{-9}	12.10	7.02×10^{-3}	8.93×10^{-3}	5.66×10^{-3}	2.20×10^{-3}

size is not limited by stability, at least in terms of a linear analysis. However, the accuracy sets a restriction on the length of the time step and, therefore, the cases were computed with various time steps.

6.3. Test case 2

The second test case is a flow over a biconvex airfoil at an angle of attack of 30°. The nominal Reynolds number based on the chord length L is 1.83×10^6. The average height of the first cell from the surface is around 14 in dimensionless units, which was posteriorly approximated from the calculated result. The grid is of the O-type and the outer boundary is $19L$ away from the airfoil surface. The number of grid points is 192×64 in the azimuthal and radial directions, respectively. As with the cylinder case, the Dirichlet condition is set in the outer boundary ghost cells and a no-slip condition at the solid wall.

In reality, the flow is highly three dimensional but here the case is computed in two dimensions. In the Adams–Bashford computation, the convergence criterion is set as previously. The Euler scheme was not used in this case. For the implicit scheme, L_2-residual of the mass

Table II. The parameters and results from the computations performed with the explicit schemes.

Reynolds number	CFL	C_{DIFF}	C_D	$C_{L\,max}$	$C_{L\,rms}$	Str	CPU time (s)
Euler							
100	0.5	1	1.3685	0.34570	0.24452	0.17021	286.26
200	0.5	1	1.3414	0.68789	0.48229	0.20292	379.21
400	0.4	1	1.4198	1.0921	0.75849	0.21740	648.72
800	0.4	1	1.4690	1.3443	0.87853	0.24063	1017.2
1600	0.3	1	1.5051	1.8200	1.0447	0.24133	1284.9
Adams–Bashford							
100	0.3	1	1.3544	0.31864	0.22466	0.17128	392.42
200	0.3	1	1.3187	0.64274	0.45476	0.19074	508.25
400	0.3	1	1.3520	1.96804	0.68330	0.21569	624.11
800	0.3	1	1.3857	1.1567	0.79783	0.23750	997.90
1600	0.2	1	1.4682	1.5056	0.97227	0.26029	1278.7

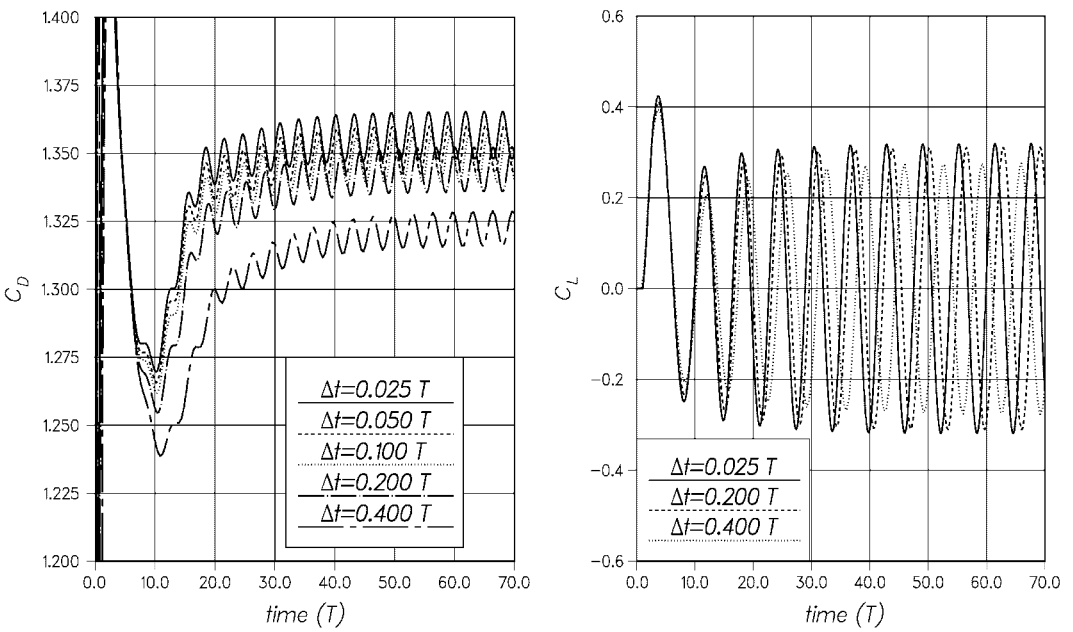

Figure 11. The drag and lift coefficient histories at $Re = 100$ with various time steps during $t = [0, 70T]$.

error was reduced to be 10^{-8} at the end of each time step, which is a decade looser than that for the cylinder case. In order to maintain stability, a third-order-upwind biased discretization for the convective terms was applied.

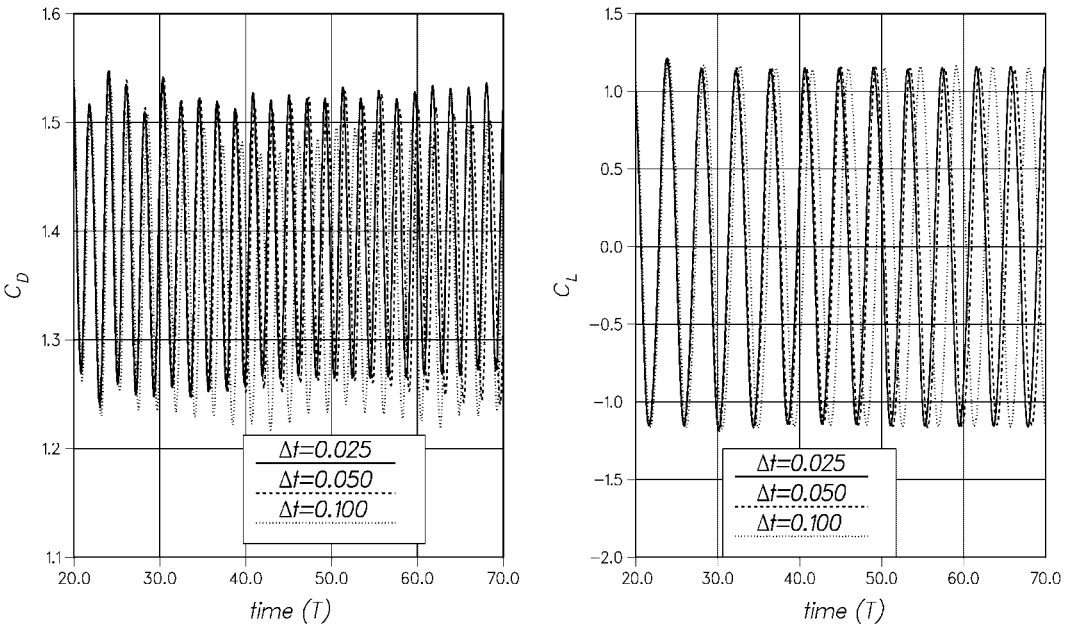

Figure 12. The drag and lift coefficient histories at $Re = 800$ with various time steps during $t = [20, 70T]$.

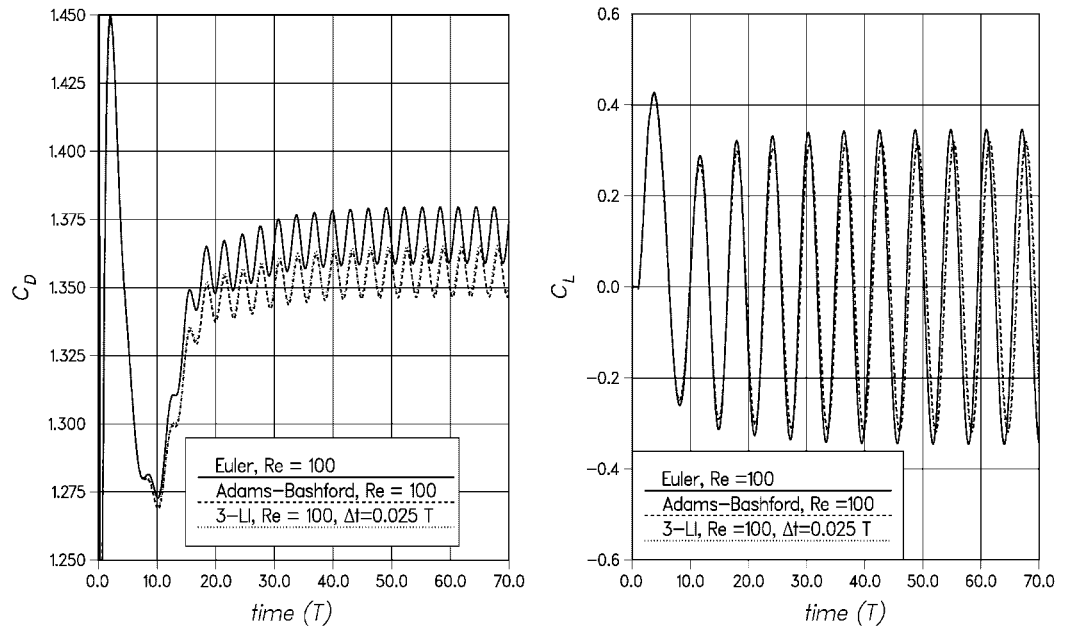

Figure 13. The drag and lift coefficient curves from the simulation with the Reynolds number of 100 during $t = [0, 70T]$.

Table III. The parameters and results from the 3-I.I computations.

Reynolds number	Δt (T)	CFL and C_{DIFF}	α_{p}	C_{D}	$C_{\mathrm{L\ max}}$	$C_{\mathrm{D\,rms}}$	Str	CPU time (s)
100	0.025	2	1.00	1.356	0.319	0.224	0.171	4752.3
100	0.050	2	0.75	1.351	0.318	0.224	0.161	3293.6
100	0.100	2	0.50	1.347	0.317	0.224	0.160	2507.7
100	0.200	2	0.50	1.343	0.311	0.221	0.160	1784.6
100	0.400	2	0.50	1.320	0.277	0.194	0.149	1038.1
200	0.025	1	1.00	1.319	0.647	0.455	0.191	5608.5
200	0.050	1	0.90	1.314	0.645	0.456	0.192	3671.6
200	0.100	1	0.60	1.313	0.643	0.456	0.193	2759.6
200	0.200	1	0.50	1.321	0.622	0.440	0.195	1983.7
400	0.025	1	0.75	1.352	0.974	0.683	0.215	6735.6
400	0.050	1	0.75	1.338	0.969	0.682	0.216	4219.8
400	0.100	1	0.60	1.324	0.966	0.675	0.217	3038.1
400	0.200	1	0.50	1.371	0.948	0.671	0.221	2166.0
800	0.025	1	0.75	1.397	1.170	0.815	0.239	6964.3
800	0.050	1	0.60	1.387	1.171	0.813	0.245	5051.7
800	0.100	1	0.50	1.362	1.169	0.823	0.227	3333.3
800	0.200	1	0.40	1.416	1.182	0.840	0.226	2346.0
1600	0.025	1	0.50	1.436	1.427	0.938	0.258	9975.7
1600	0.050	1	0.40	1.421	1.458	0.928	0.245	6966.2
1600	0.100	1	0.30	1.417	1.413	0.910	0.230	5075.0
1600	0.200	1	0.20	1.385	1.300	0.876	0.226	4085.0

6.4. *Results*

With the explicit schemes, the CFL number was set as large as the stability permitted. The viscous time-step parameter C_{DIFF} does not seem to have any effect, and it was set to be one in each simulation. The Euler scheme can utilize a slightly larger CFL number, as seen in Table II. With the implicit method, the time-step size was varied over a wide range from 0.025 to $0.4T$. The drag and lift coefficient histories are seen in Figure 11 in the case of $Re=100$. Immediately it can be observed that the time-step size $0.4T$ is too long because of the strong deviation in the results from the other computations. With the case $\Delta t=0.2T$, the averaged values are close to the values from the simulation with the smallest time step. The dimensionless cylinder shedding frequency, the Strouhal number, is defined as fD/U_{∞}, and it differs somewhat from the other simulations. In Figure 12, the force coefficient histories are shown for the case $Re=800$ with different time-step sizes. Some difference can again be seen in the Strouhal number but the averaged quantities coincide relatively well. The computations and the results are collected in Table III. Figures 13–17 show the drag and lift coefficient curves versus time computed with different methods. The result of the implicit method is from the runs with the smallest time step $\Delta t=0.025T$.

As a general overview, one can remark that the results from the Euler computations deviate most from the others. These deviations seem to increase with an increasing Reynolds number.

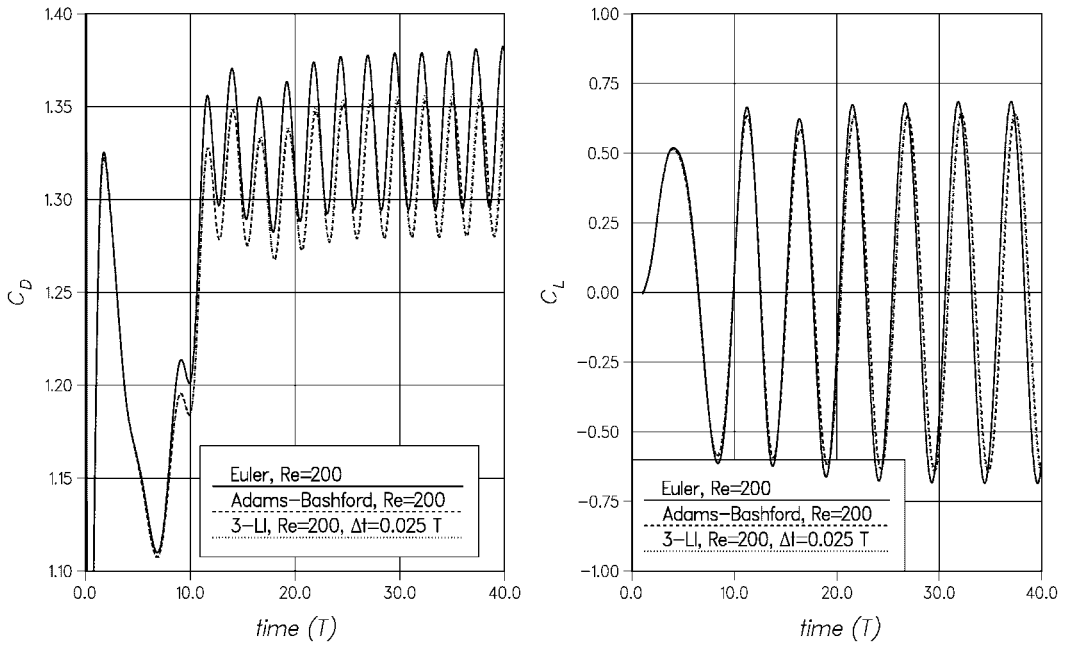

Figure 14. The drag and lift coefficient curves from the simulation with the Reynolds number of 200 during $t = [0, 40T]$.

The results from the second-order accurate simulations are practically identical, except for the case $Re = 1600$.

In Figures 18 and 19, the mean drag coefficient C_D and the Strouhal number are presented. The Strouhal number 0.2 means that the shedding cycle takes place during the time in which the free stream moves five cylinder diameters. From Reference [11] one can find measured values and other numerical results for comparison. In general, with the Reynolds numbers of 100 and 200, all the quantities given above coincide well with the earlier results, and most deviations occur with the first-order accurate Euler method, as stated before. When the Reynolds number is 400 or larger, the deviations from the measured values grow. The measured values for the mean drag coefficient vary around 1.2 between the Reynolds numbers of 400 and 1000 and decrease down to 0.9 as $Re \approx 4000$. In the present results, C_D grows from 1.35 to about 1.5. The Strouhal number should be relatively constant between 0.20 and 0.21 [11], whereas in the present simulations it increases from 0.21 to 0.25.

These deviations result from the fact that there is a transition around $Re \approx 180$, where the wake becomes three-dimensional. Mittal and Balachandar [13] have simulated a flow over a cylinder at $Re = 525$. After a transition from two to three-dimensional flow, the mean C_D dropped from 1.44 to 1.24 and the amplitude of C_L dropped from 1.21 to 0.64. In a two-dimensional flow, the average base pressure in the wake appears to be lower than in a three-dimensional flow.

In the present computations, the explicit methods appear to be faster, as seen in Figure 20. The computations were performed in an SGI R10000 175 MHZ processor. With $Re = 100$,

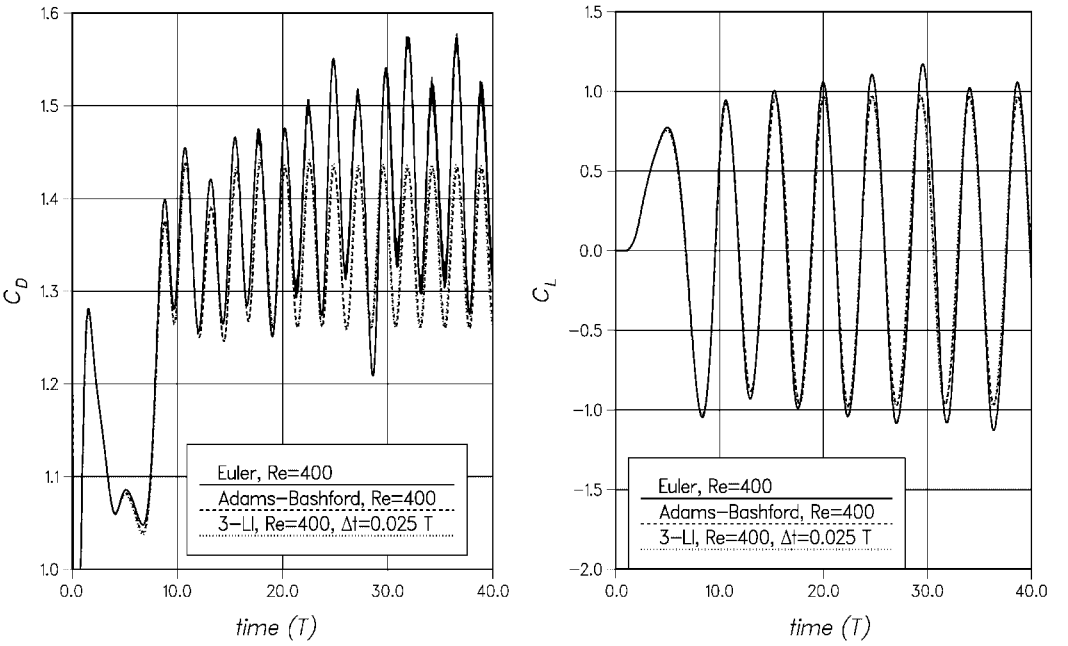

Figure 15. The drag and lift coefficient curves from the simulation with the Reynolds number of 400 during $t=[0,40T]$.

the explicit methods are faster than the implicit one by a factor of 5–10 depending on the time-step size and convergence limits used with the implicit computation. As the Reynolds number was increased to 1600, the factor is slightly decreased but the explicit methods are still from four to eight times faster. Figure 21 shows the number of subiterations used by the implicit scheme with various time steps.

Typical time-step sizes used in this range of Reynolds number lie between 0.01 and $0.05T$ in the case of a vortex-shedding cylinder flow and an implicit method [11, 14]. In the present calculations, the explicit methods use time steps from $0.017T$ ($0.01T$ Adams–Bashford) to $0.003T$ as the Reynolds number was increased from 100 to 1600, as seen in Figure 22.

In the case of the flow over biconvex airfoil, the computation was run during the time of $200T$, where $T=U_\infty/L$. The velocities $u/U_\infty, v/U_\infty$ and the fluctuations uu/U_∞^2, vv/U_∞^2 and uv/U_∞^2 are gathered during the last $190T$.

The Adams–Bashford scheme remains stable with CFL = 1. The average number of time steps is 18 584 during $1T$. The time-step length varies greatly during the simulation. The longest steps, taken at the maximum of the lift, are longer than the smallest ones by a decade. The results are plotted and the statistics are gathered at the equal intervals of $5\times10^{-4}T$.

The implicit 3-LI-method requires also a small time-step size of $0.001T$ to converge properly. The average number of subiterations within the time step is 7.8 to reach the convergence limit that is 10^{-8} for the L_2-norm of the mass error. The number of subiterations varies greatly too, from 3 to 30. The underrelaxation parameter α_p for the pressure must be set down to the value of 0.1 to gain convergence. The force coefficient histories during $t=[70T,100T]$

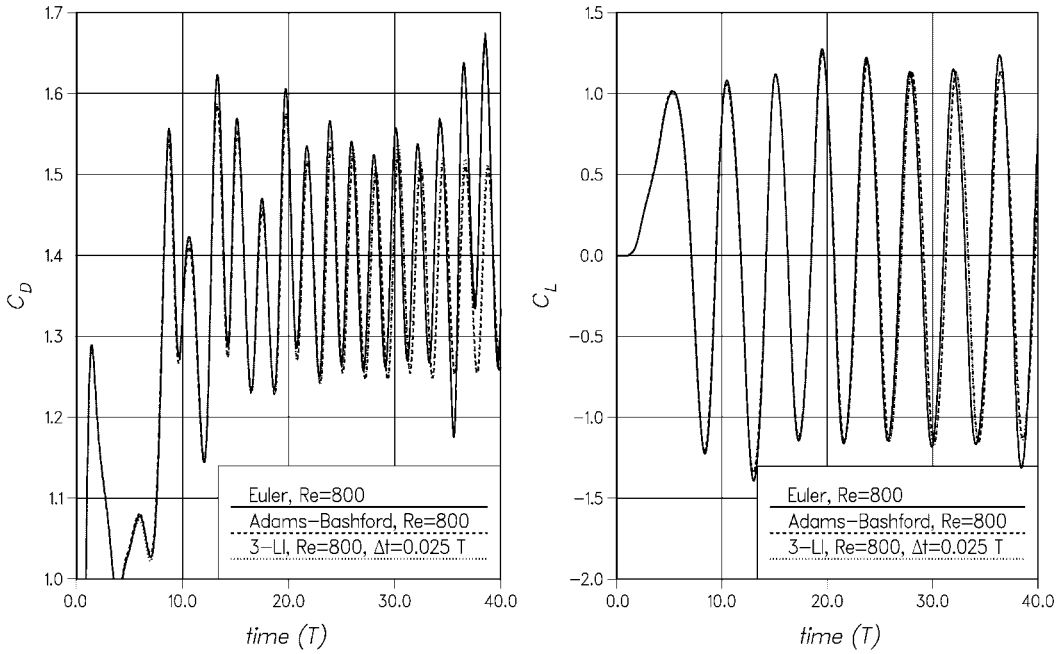

Figure 16. The drag and lift coefficient curves from the simulation with the Reynolds number of 800 during $t = [0, 40T]$.

are shown in Figure 23. The averaged drag and lift coefficients are 1.201 and 1.797 from the Adams–Bashford computation and 1.192 and 1.804 from the 3-LI computation. These averages changed approximately $\pm 1\%$ during the last $100T$. The averaged velocities and the Reynolds stresses are shown in Plates 2–6. The total CPU times measured in SGI R10000 250 MHz processors are 153 950 and 162 810 s for explicit and implicit computations, respectively. The implicit method requires 6% more CPU time and judging by the previous convergence tests, if the mass error reduced a decade further with 3-LI method, the computational effort would increase by approximately 50%.

7. CONCLUSIONS AND FUTURE WORK

The explicit Euler and Adams–Bashford methods appeared to be faster than the implicit SIMPLE-based one in the present comparison. The implicit method allows the time step to be lengthened beyond CFL = 1, but the number of iterations within the time step also grows. With the largest time step applied, the explicit methods are five times faster than the implicit ones at $Re = 100$. At the highest Reynolds number, $Re = 1600$, the factor is four. The maximum local CFL number with this time step is approximately 30 at $Re = 1600$, so the step is too long to capture the fine structure in a turbulent flow. As the step size is decreased by one decade, the explicit methods are faster by a factor of ten at $Re = 100$. At the Reynolds number of 1600, the factor is slightly lowered to eight. The results obtained with the Reynolds numbers of 400 and higher deviate from the measured due to the three dimensionality of the

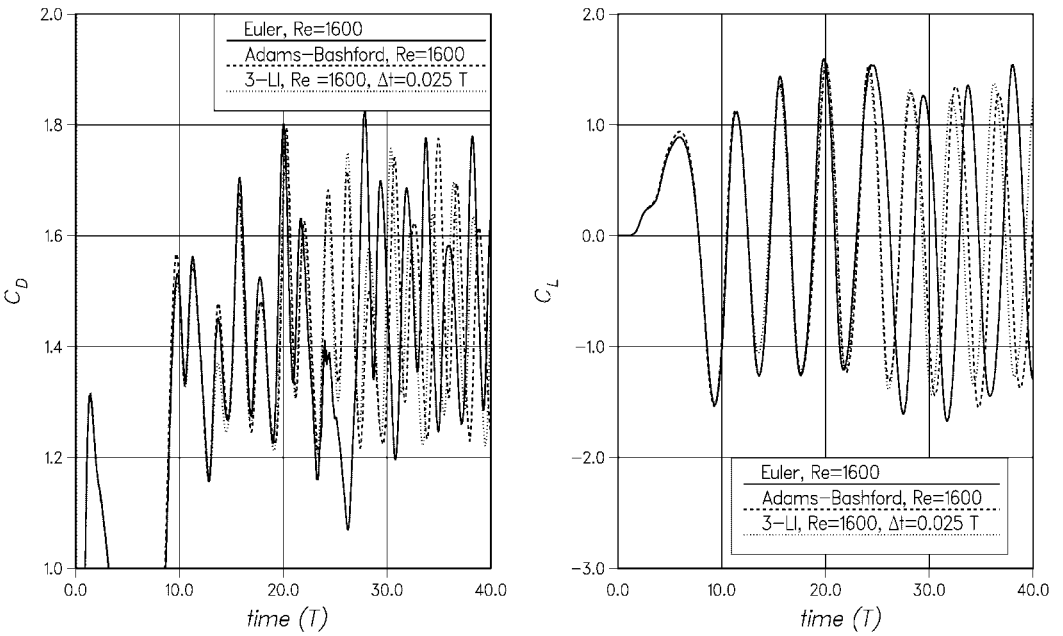

Figure 17. The drag and lift coefficient curves from the simulation with the Reynolds number of 1600 during $t = [50, 70T]$.

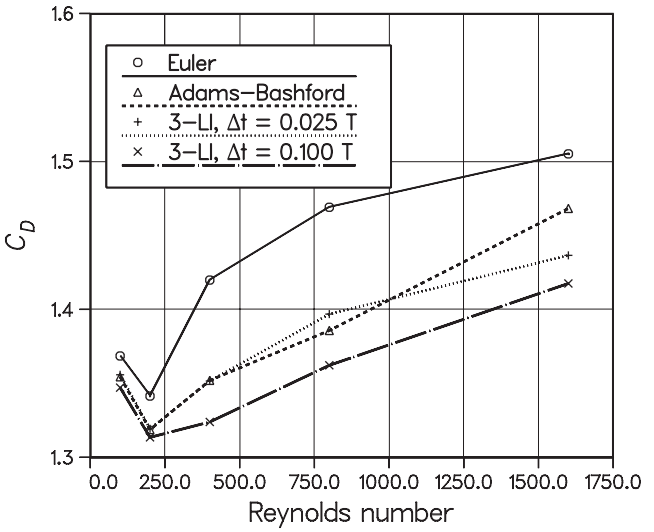

Figure 18. The mean drag coefficient versus the Reynolds number.

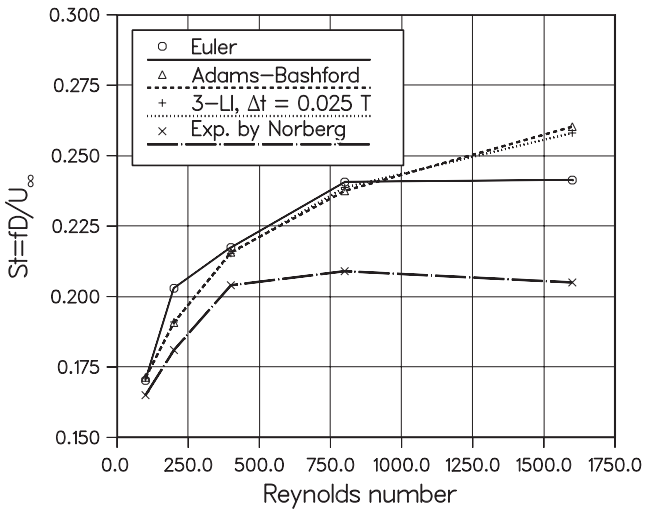

Figure 19. The Strouhal number versus the Reynolds number.

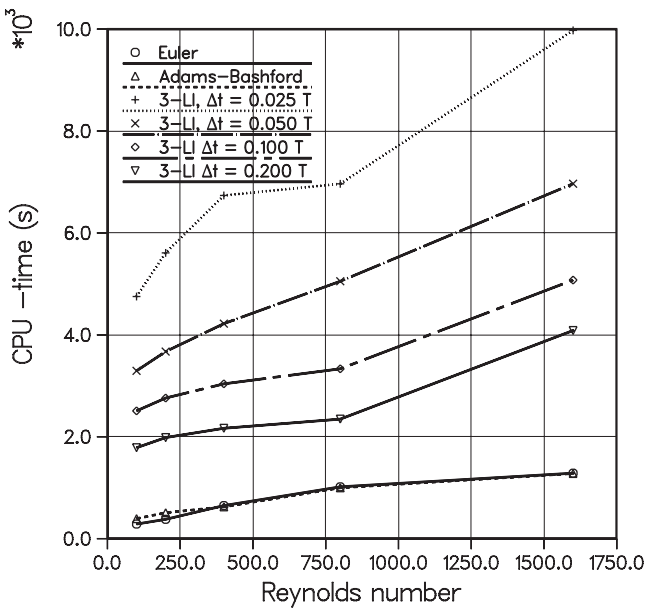

Figure 20. Total CPU times required by the simulations. CPU times are measured in an SGI R10000 175 MHz processor.

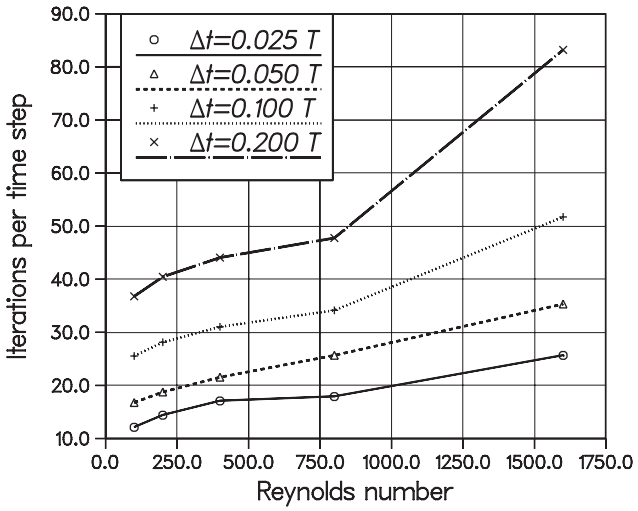

Figure 21. The number of subiterations used by the implicit scheme.

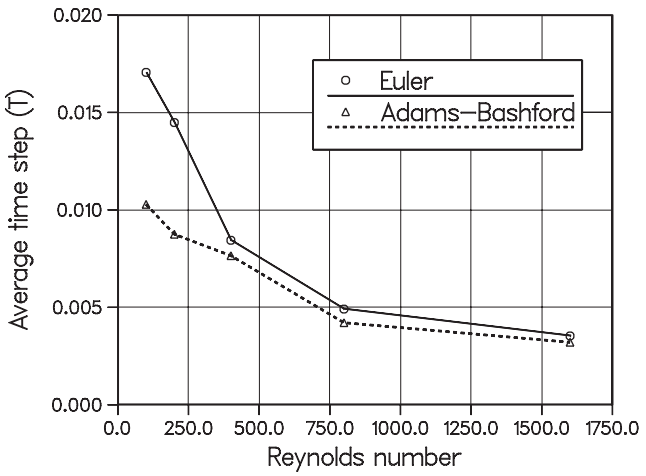

Figure 22. The average time-step size used by the explicit schemes.

real flow. However, this hardly affects the comparison between the methods used and their computational efficiency. At the higher Reynolds number, the computational mesh includes small cells near the solid boundaries that restrict the time-step length. An implicit method is able to use a time-step size that is about 20 times larger than that of an explicit one. The force coefficients and the statistically gathered first and second moments are practically identical from both calculations. Owing to the subiterations and the solution of the implicit momentum equations, the computational time is still slightly more than that of the explicit calculation. The difference is negligible compared to the low-Reynolds-number cases, however. The present

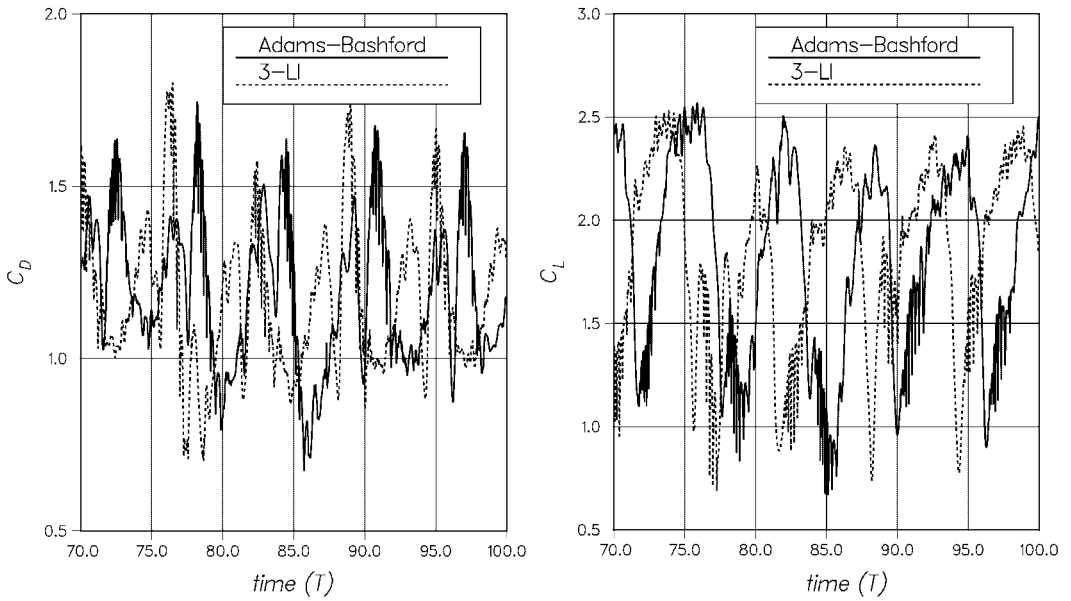

Figure 23. The drag and lift coefficient curves from the simulation of the flow over the biconvex airfoil at the Reynolds number of 1 830 000 during $t = [70T, 100T]$.

implicit method is based on the SIMPLE algorithm, which can possibly be improved by different derivative schemes like SIMPLEC or PISO. Another important issue, which has been omitted in this study is parallelization. In practice, most turbulent time-dependent cases are computationally highly intensive tasks which are solved in parallel systems. A common approach is to divide the physical solution domain into subdomains and assign each subdomain to one processor. The amount and frequency of data exchanged between processors affects the performance. For instance, the solution of the elliptic Poisson equation might be an intensive task in terms of data exchange, if solved in a subdomain parallelization scheme. The effect on the performance may differ depending on the computational algorithm used.

ACKNOWLEDGEMENTS

This research project has been funded by the Academy of Finland whose support is gratefully acknowledged.

REFERENCES

1. Hirsch C. *Computational Methods for Inviscid and Viscous Flows*, vol. 2 *of Numerical Computation of Internal and External Flows*. John Wiley & Sons Ltd: Chichester, 1990. ISBN 0-471-92351-6.
2. Choi H, Moin P, Kim J. Direct numerical simulation of turbulent flow over riblets. *Journal of Fluid Mechanics* 1994; **255**:533–555.
3. Harlow FH, Welch JE. Numerical calculation of time-dependent viscous incompressible flow of fluid with free surface. *The Physics of Fluids* 1965; **8**(12):2182–2189.
4. Chorin AJ. Numerical solution of the Navier–Stokes equations. *Mathematics of Computation* 1968; **23**: 341–354.

5. Patankar SV. *Numerical Heat Transfer and Fluid Flow*. Hemisphere: Washington, D.C, 1980. ISBN 0-89116-522-3.
6. Rhie CM, Chow WL. Numerical study of the turbulent flow past an airfoil with trailing edge separation. *AIAA Journal* 1983; **21**(11):1525–1532.
7. Miettinen A. A study of the pressure correction approach in the colocated grid arrangement. *Technical Report No. 110*, Helsinki University of Technology, Laboratory of Applied Thermodynamics, 1997. ISSN 1237-8372.
8. Burden RL, Faires D. *Numerical Analysis* (5th edn). PWS Publishing Company, Boston, MA, 1993. ISBN 0-534-93219-3.
9. Kim J, Moin P. Application of a fractional-step method to incompressible Navier–Stokes equations. *Journal of Computational Physics* 1985; **59**:308–323.
10. Hoffren J. Time-accurate schemes for a multi-block Navier–Stokes solver. *Report A-14*, Helsinki University of Technology, Laboratory of Aerodynamics, 1992. ISBN 951-22-1350-8.
11. Braza M, Chassaing P, Ha Minh H. Numerical study and physical analysis of the pressure and velocity fields in the near wake of a circular cylinder. *Journal of Fluid Mechanics* 1986; **165**:79–130.
12. Davidson L. Implementation of a large eddy simulation method applied to recirculating flow in a ventilated room. *Technical Report*, Department of Building Technology and Structural Engineering, Aalborg, 1996. ISSN 1395-7953-R9611.
13. Mittal R, Balachandar S. Effect of three-dimensionality on the lift and drag of nominally two-dimensional cylinders. *Physics of Fluids* 1995; **7**(11):1841–1865.
14. Sohankar A, Norberg C, Davidson L. Low-Reynolds-number flow around a square cylinder at incidence: study of blockage, onset of vortex shedding and outlet boundary condition. *International Journal for Numerical Methods in Fluids* 1998; **26**:39–56.

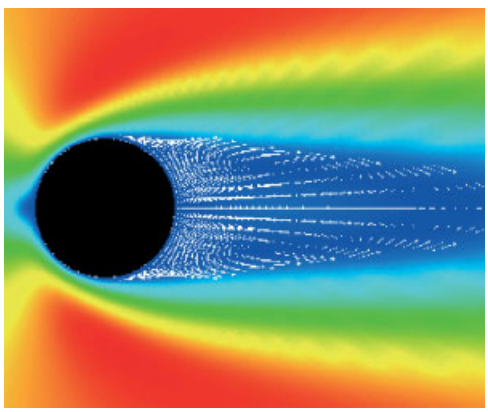

Plate 1. Velocity vectors in the re-circulation zone. The Reynolds number is 40.

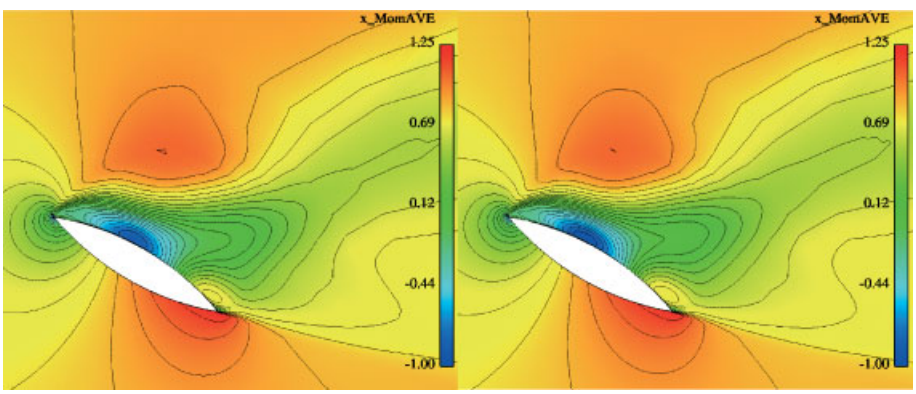

Plate 2. The averaged velocity u/U_∞. On the left, the Adams–Bashford solution, and on the right the 3-LI solution.

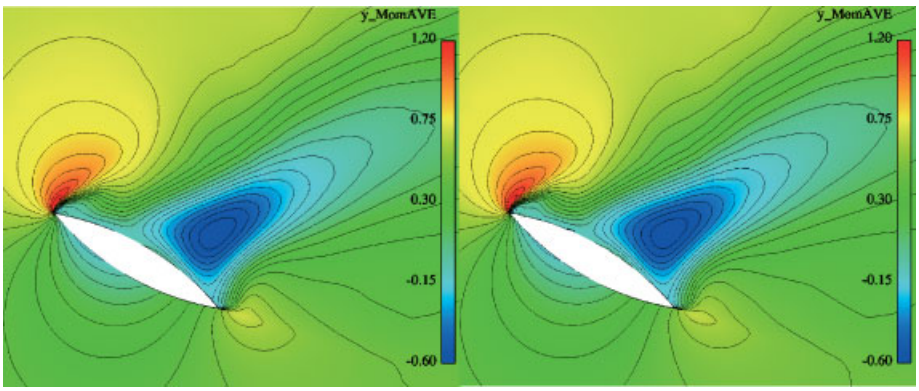

Plate 3. The averaged velocity v/U_∞. On the left, the Adams–Bashford solution, and on the right the 3-LI solution.

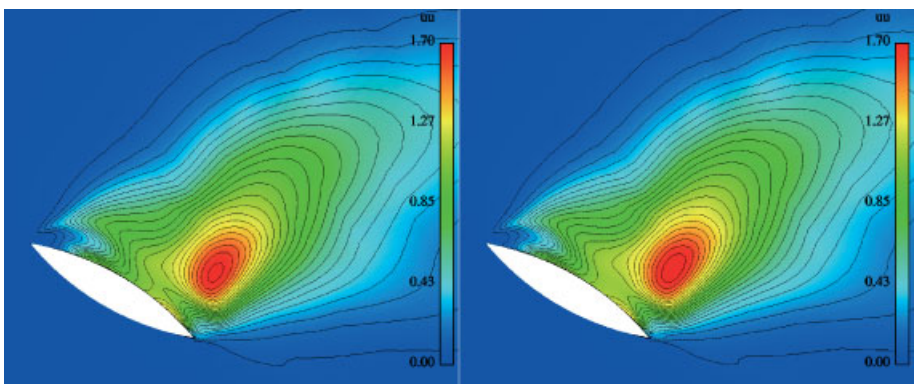

Plate 4. The Reynolds stress uu/U_∞^2. On the left, the Adams–Bashford solution, and on the right the 3-LI solution.

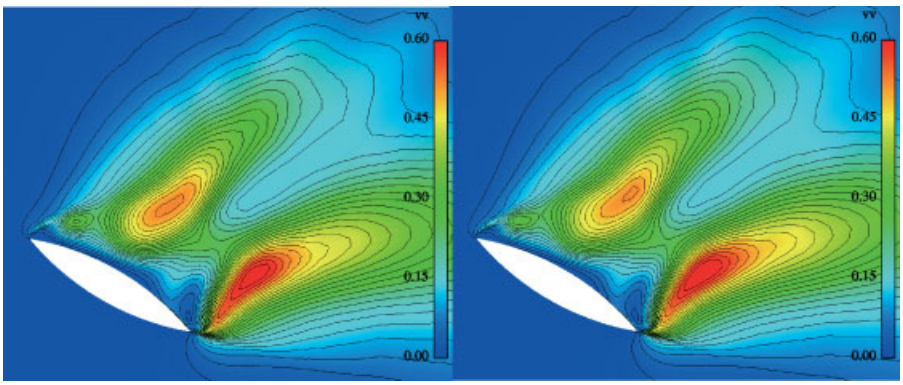

Plate 5. The Reynolds stress vv/U_∞^2. On the left, the Adams–Bashford solution, and on the right the 3-LI solution.

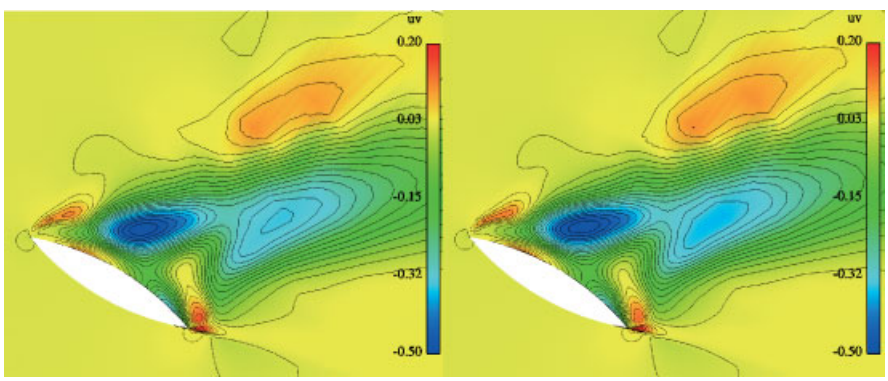

Plate 6. The Reynolds stress uv/U_∞^2. On the left, the Adams–Bashford solution, and on the right the 3-LI solution.